Large Area Monolithic Organic Solar Cells

Hui Jin*, Chen Tao, Mike Hambsch, Almantas Pivrikas, Marappan Velusamy, Muhsen Aljada, Yuliang Zhang, and Paul L. Burn*, Paul Meredith*

Centre for Organic Photonics and Electronics (COPE), The University of Queensland, Brisbane, QLD, Australia 4072

ABSTRACT

Although efficiencies of > 10% have recently been achieved in laboratory-scale organic solar cells, these competitive performance figures are yet to be translated to large active areas and geometries relevant for viable manufacturing. One of the factors hindering scale-up is a lack of knowledge of device physics at the sub-module level, particularly cell architecture, electrode geometry and current collection pathways. A more in depth understanding of how photocurrent and photovoltage extraction can be optimised over large active areas is urgently needed. Another key factor suppressing conversion efficiencies in large area cells is the relatively high sheet resistance of the transparent conducting anode - typically indium tin oxide. Hence, to replace ITO with alternative transparent conducting anodes is also a high priority on the pathway to viable module-level organic solar cells. In our paper we will focus on large area devices relevant to sub-module scales – 5 cm × 5 cm monolithic geometry. We have applied a range of experimental techniques to create a more comprehensive understanding of the true device physics that could help make large area, monolithic organic solar cells more viable. By employing this knowledge, a novel transparent anode consisting of molybdenum oxide (MoO_x) and silver (Ag) is developed to replace ITO and PEDOT-free large area solar cell sub-modules, acting as both a transparent window and hole-collecting electrode. The proposed architecture and anode materials are well suited to high throughput, low cost all-solution processing.

Keywords: photovoltaics, organic solar cells, polymer, module, monolithic, transition metal oxide, transparent anode

1. INTRODUCTION

Recent progress in conjugated polymer solar cells (PSCs) has given rise to "small" laboratory-scale devices with efficiencies > 10%.[1] Critically, these competitive conversion efficiencies are yet to be translated to large devices with module-scale active areas. This is in part due to architectural limitations and the use of indium tin oxide (ITO) as the transparent conducting electrode (TCE).

The reliance upon ITO as the TCE of choice has unfortunately hindered the scaling of OSCs to sub-module and module levels for multiple reasons: firstly cost, but it also appears that the sheet resistance of ITO prohibits effective current collection over collection pathways (the shortest linear distance to an electrode) of more than a few cms.[2,3] Besides, for many doped metal oxides (including ITO) an inherent trade off exists between doping (to achieve low resistance) and transparency.[4,5] This of course leads to an obvious problem for solar cells: the number of photons transmitted into the active junction through the TCE must be optimised, and yet in a device dominated by series resistance the maximum photocurrent needs to be extracted. Although several groups have studied these effects in combination with electrode geometry for serially connected strip architectures, there has been relatively little focus on monolithic devices with collection pathways greater than a few cms. From a manufacturing perspective, the monolithic architecture is undoubtedly preferrable since it can lead to good utilisation of the substrate and simplified processing. Therefore, irrespective of whether ITO becomes the dominant commercial TCE in organic solar cells, we must develop a more in depth understanding of how photocurrent and photovoltage extraction can be optimised over large active areas at the sub-module and module levels. In this work, the device physics of 5 cm × 5 cm monolithic organic solar cells based on a blend of the model donor polymer poly(3-*n*-hexylthiophene) (P3HT) and the electron acceptor [6,6]-phenyl-C_{61}-butyric acid methyl ester ($PC_{60}BM$) is investigated with particular emphasis on collection efficiency as a function of electrode geometry.

* h.jin1@uq.edu.au; p.burn2@uq.edu.au; meredith@physics.uq.edu.au

Optoelectronic Devices and Integration IV, edited by Xuping Zhang, Hai Ming, Joel M. Therrien,
Proc. of SPIE Vol. 8555, 855522 · © 2012 SPIE · CCC code: 0277-786/12/$18
doi: 10.1117/12.999270

Further, by employing the knowledge of device physics of ITO-based monolithic sub-modules, we propose efficient, large area organic (polymer) solar cells fabricated without ITO or poly(3,4-ethylenedioxythiophene)polystyrene sulfonic acid (PEDOT:PSS). We employ a transparent top anode consisting of molybdenum oxide (MoO_x) and silver (Ag) in an "inverted-illumination" geometry in conjunction with a thick aluminium bottom contact. The optimised MoO_x-Ag-MoO_x stack (MAMS) has an optical transmission of 80% at the wavelength of 520 nm, sheet resistance of ~ 5 ohm sq^{-1} and yields conversion efficiencies in 25 cm^2 "sub-modules" of 3.2% - outperforming the equivalent conventional ITO/PEDOT:PSS devices. Critically, the device is not a serially-connected array of thin strips, but contains a single monolithic 5 cm × 5 cm photoactive area. The replacement of both ITO and PEDOT:PSS are critical steps on the pathway to commercially and technically viable organic solar cells, and the proposed architecture is well suited to high throughput, low cost all-solution processing.

2. DEVICE PHYSICS IN MONOLITHIC, LARGE-AREA SOALR CELLS

A series of large area monolithic (i.e., not serially connected strip) organic solar cells were prepared on ITO-coated glass substrates with the structure of ITO/PEDOT:PSS/P3HT:PC_{60}BM/Al.[6] Three electrode geometries were implemented to achieve centrally symmetric and diagonally symmetric collection architectures with device active areas of 5 cm × 5 cm. Schematic illustrations of the devices with the three electrode geometries (G_O, G_M and G_L) are shown in **Figure 1**a-c, respectively. The top light grey parts represent metal aluminum (Al) cathodes, and the side Al bars are connected with the bottom ITO as anode contacts. The round and square symbols represent the contact positions for positive and negative probes, respectively. As such, all the round symbol positions were at equal positive potential and all the square symbol positions at equal negative potential. The contact area of the probe head was approximately 1.0 mm^2. The collection circuit around the monolithic device does compromise the geometric fill factor, but in practise it would be integrated into the module architecture as is the case with inorganic solar cells.

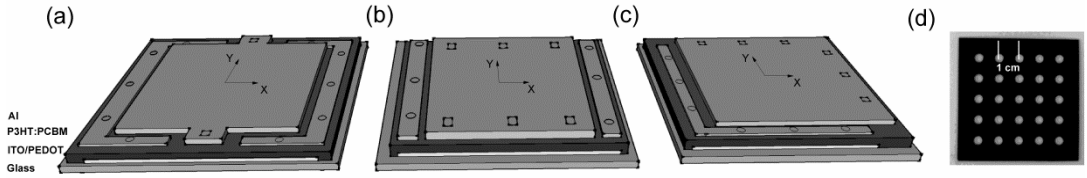

Figure 1 A schematic illustration of the three electrode geometries G_O (a), G_M (b), and G_L (c) used in this study, and a photograph of the illumination mask used for device mapping (d).

Due to the relatively high sheet resistance of ITO, it has been reported that power loss from the ITO becomes the only area-scaling parameter.[7] Since the resistance of Al is negligible, the voltage drop across the Al cathode is assumed to be zero. Therefore, the resistance to the collection of positive charge carriers over the ITO electrode area determines the electric field distribution and the current flow as a whole. Both G_O and G_M are centrally symmetric architectures with surrounding and two-side extraction bars respectively, while G_L is a diagonally symmetric design with corner-type bars.

Figure 2 shows representative current density versus voltage (*J-V*) characteristics of devices in the three electrode geometries (G_O, G_M and G_L) under illumination of AM 1.5. On average the conversion efficiencies of the G_O, G_M and G_L geometries were 1.0%, 0.9% and 0.75%, respectively, with this P3HT:PC_{60}BM combination. For perspective, we routinely achieve conversion efficiencies of order 3.0-3.5% with this material combination on lab-scale devices (0.2 cm^2). The parameters affected mostly by the electrode geometry are short circuit current density (J_{SC}) and the device series resistances (R_S) extracted from the *J-V* slope at open circuit, which are reduced and increased, respectively, by 37% from the devices G_O and G_M to G_L. The higher internal resistance caused by the diagonally symmetric design G_L likely leads directly to the loss of J_{SC}. However, only a small difference (< 0.5 mA cm^{-2}) is observed between the G_O and G_M devices confirming that the ITO collection length in the dimension of the carrier flow dominates the internal resistance. We would therefore surmise that G_O is a suitable architecture for monolithic solar cell sub-modules since it can produce more current, while G_M is more suitable for serially-connected stripe modules due to its simple design.

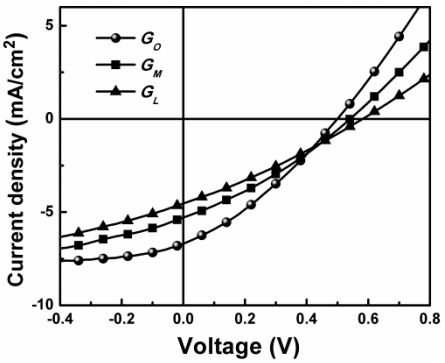

Figure 2 Typical current density-voltage (*J-V*) characteristics for the three electrode geometries (G_O, G_M and G_L) with a photoactive area of 25 cm^2. These characteristics were measured under AM1.5G illumination conditions using a calibrated solar simulator with irradiation intensity of ~100 mW cm^{-2}.

In order to explain the performance variation between the three geometries, the currents within the electrode area were mapped using a mask with 25 apertures each of area of 0.28 cm^2 (Figure 1d). The centre aperture in the mapping mask was defined as (0, 0) in an X-Y coordinate system and the interval distance between adjacent aperture centres was 1.0 cm. Only one aperture was open in each measurement, so the total map represented 25 measurements and data points. **Figure 3**a-c show the J_{SC} dependence on the illumination position for typical devices in G_O, G_M and G_L electrode geometries. For G_O and G_M the current only reduces slightly when the beam is in the central area and there is a higher current around the periphery. The current values in G_M at the two edges without Al side bars for hole collection are lower, which explains the small overall reduction in J_{SC} for G_M versus G_O. However, in the device G_L the current drops by a factor of two when the beam is positioned in the corner diagonally opposite the corner of the collection electrode bars. In contrast, the open-circuit voltage (V_{OC}) is independent of the illumination position as shown in Figure 3d-f. Therefore, one can say that the spatial distribution of J_{SC} is determined by the effective series resistance in G_L architecture devices. The current at (-2, -2) is twice that at (2, 2), which means the ITO collection path length of 5.6 cm between these two points causes the series resistance to double.

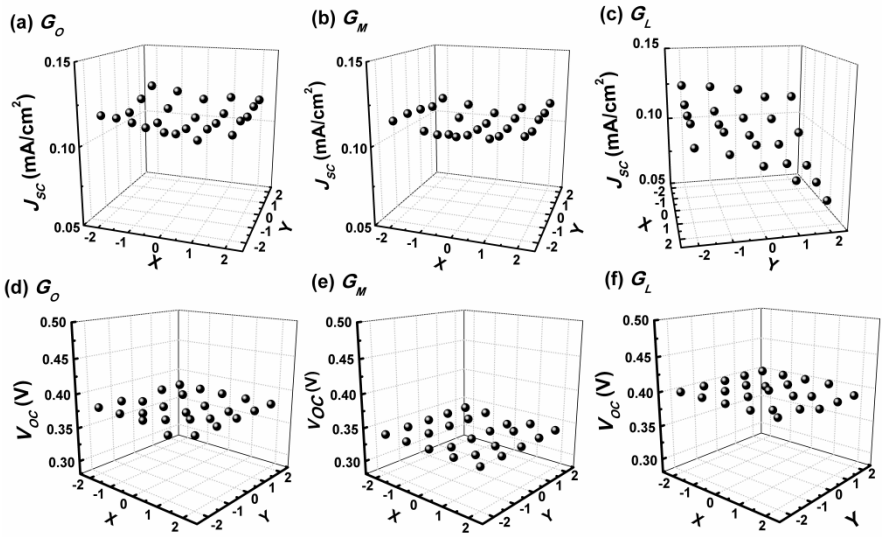

Figure 3 Variation of photovoltaic parameters J_{SC} (a-c), normalized to 25 cm^2 and V_{OC} (d-f) as a function of illumination position for the three electrode geometries G_O, G_M and G_L.

Further confirmation of this geometric effect was obtained by constructing a 2D model for the different electrodes in COMSOL and modeling the current density in the ITO. A detailed description of the modeling parameters can be found in the 'Experimental section'. Instead of applying a test source at the discrete mask locations and simulating the effect, we applied a test voltage and solved Poisson's equation for the respective electrode geometries. **Figure 4**a-c shows the

normalized (lateral) current density for the different electrodes. We note good agreement between the general shape of the current density in the ITO sheet and the measured J_{SC} profile. For G_M and G_O the minimum occurs at the centre of the ITO. For G_L we observe a profile with diagonal symmetry; with the minimum at the corner (-2.5, -2.5) being an artifact of the simplification in the modeling in applying the bias along the edges. Overall the results are consistent with the view that the current decreases further away from the test voltage source due to resistive losses, and therefore accounts for the variations we observe in the J_{SC} profile for the different electrode geometries.

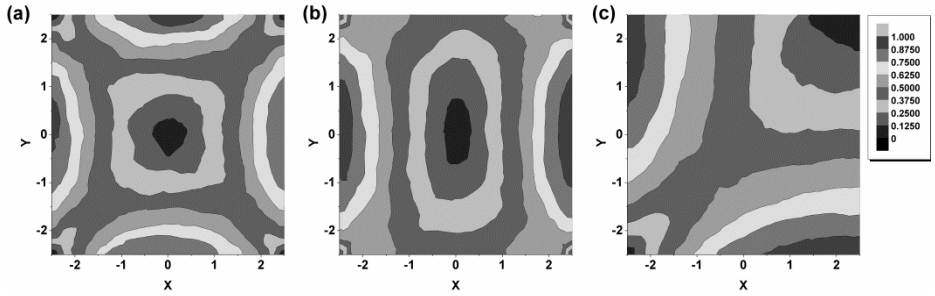

Figure 4 COMSOL modeled current density in the ITO anode for different electrode geometries G_O (a), G_M (b) and G_L (c).

3. ITO-&-PEDOT-FREE MONOLITHIC SUB-MODULES

To be an effective transparent conducting anode, the MAMS we have developed has met three requirements: first, the contact between the photoactive layer and the stack is ohmic.[8] The thin MoO_x layer adjacent to the photoactive layer (M1 in Figure 1a) serves this function when its thickness is less than 10 nm[9]; second, the essential low sheet resistance is achieved by a thin Ag interlayer. Thicker metal films can provide higher conductivity but lead to lower optical transmittance and as we describe later, this is a delicate optimization balance; finally, appropriate design has been used to maximise the optical field density in the photoactive layer by subtle manipulation of coherent optical interference effects.[10-12] In this regard, the outer MoO_x layer (M2 in **Figure 5**) was introduced as a light coupling layer to tune the optical properties of the MAMS and particularly mitigate deleterious reflections caused by the large mismatch of refractive indices at the Ag/air interface.

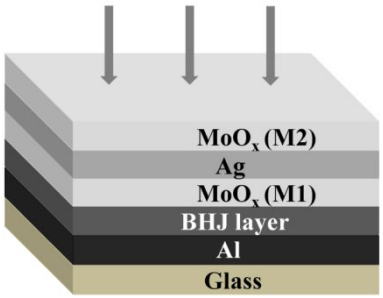

Figure 5 Device structure of a MoO_x-Ag-MoO_x stack (MAMS) inverted illumination solar cell.

To ensure the optimal balance between transparency and resistivity of the stack the optimal thicknesses of each layer in the MAMS were simulated via the Fresnel matrix method. **Figure 6**a shows the excellent agreement between the simulated and experimental optical transmittance spectra of the optimal MAMS with thicknesses M1 = 5 nm; Ag = 13 nm; M2 = 40 nm. The MAMS configuration was arrived at by simulating and measuring both the transmittance and sheet resistance of different layer thickness combinations, and by considering the optical interference effects to maximize field density and reduce reflection losses. The use of a 13 nm Ag film gave a sheet resistance of ~ 5 ohm sq^{-1} (Figure 6b) for the MAMS, which is critical for fabricating large-area organic solar cells, and is lower than standard ITO. We also note that the transmittance of the optimized stack is comparable with that of ITO-glass, and further that it matches well with the spectral window (350 nm to 800 nm) required for efficient solar harvesting with most current acceptor-donor combinations. For example, Figure 6a shows the absorption spectra of the bulk heterojunction blends of P3HT:PC_{60}BM and poly[N-9''-heptadecanyl-2,7-carbazole-alt-5,5-(4',7'-di-2-thienyl-2',1',3'-benzothiadiazole)]:[6,6]-phenyl-C71-butyric acid methyl ester (PCDTBT:PC_{70}BM) used in this work.

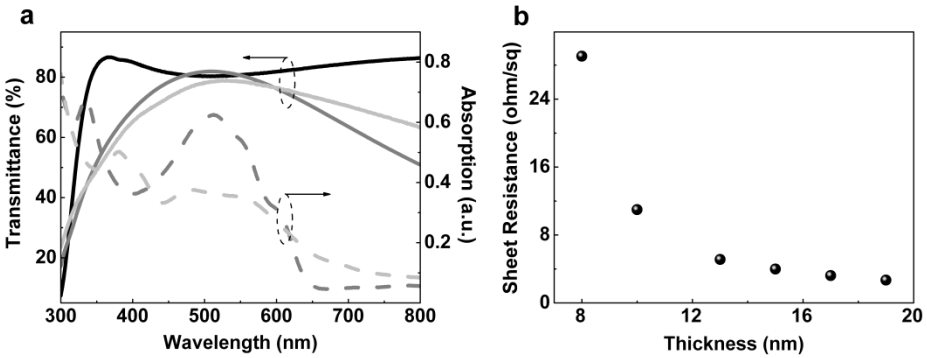

Figure 6 (a) Simulated (solid dark gray) and experimental optical transmittance spectra (solid light gray) of the optimal MAMS structure with thicknesses M1 = 5 nm; Ag = 13 nm; M2 = 40 nm, compared with transmittance spectrum of ITO film (solid dark). Absorption spectra of the P3HT:$PC_{60}BM$ (dash dark gray) and PCDTBT: $PC_{70}BM$ (dash light gray) films are also shown. (b) Sheet resistance of the MAMS electrode as a function of the thickness of the Ag interlayer.

To optimize the photoactive layer thickness, the spatial distribution of the optical field ($|E|^2$) through the whole cell and the exciton generation rates across the photoactive layer were also calculated for a range of thicknesses known to be suitable for P3HT:$PC_{60}BM$ and PCDTBT:$PC_{70}BM$ blends. **Figures 7**a and 7b show the optical field intensity for three different photoactive layer thicknesses at wavelengths of 520 and 555 nm for the P3HT:$PC_{60}BM$ (a: 90 nm; 110 nm; 130 nm) and PCDTBT:$PC_{70}BM$ (b: 80 nm; 110 nm; 140 nm) blends, respectively. The spatial distribution of the exciton generation rate for these configurations are shown in Figures 7c and 7d although in this case we have integrated over the 300 - 900 nm spectral window to capture the entire response. Due to interference effects that are dependent upon all layer thicknesses the calculated $|E|^2$ for the whole structure and the exciton generation rate for the active layer vary, with the variations being interrelated. To a reasonable approximation the exciton generation rate at a particular position inside the photoactive layer is proportional to $|E|^2$.[11] In a bulk heterojunction organic solar cell, a high light intensity in the vicinity of the organic/electrode interface is suggested to lead to a reduction in photocurrent due to exciton quenching.[13] Therefore, the maximum of the optical field and hence the peak of exciton generation should be located in the middle of the active layer. Although the number of photogenerated excitons is highest in the case of 90 and 80 nm thick layers for P3HT:$PC_{60}BM$ and PCDTBT:$PC_{70}BM$, respectively, the optimal thickness for both composites was 110 nm due to the exciton quenching effects.

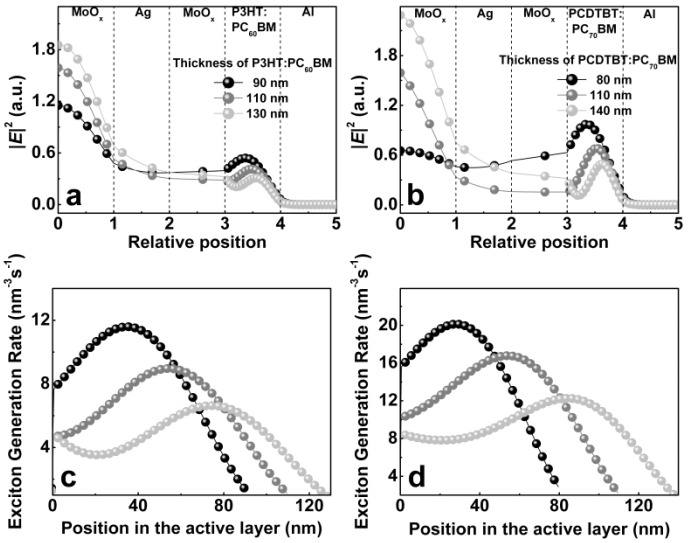

Figure 7 Calculated distribution profiles for the optical field intensity through the complete MAMS cells with P3HT:$PC_{60}BM$ (a) and PCDTBT:$PC_{70}BM$ (b) at the wavelengths of 520 and 555 nm, respectively. The

calculated distribution profiles of exciton generation rate across the photoactive layers in the MAMS cells with P3HT:$PC_{60}BM$ (c) and PCDTBT:$PC_{70}BM$ (d).

Based upon these insights, we fabricated devices of each active area dimension: 0.2 cm^2 as our standard laboratory scale to demonstrate the working principles of the optimization; 2.9 cm^2 to understand how the reduced sheet resistance of the MAMS may impact large area device performances; and 25.0 cm^2 (a monolithic 5 cm × 5 cm device) to assess the performance at a "sub-module" level in comparison to a standard ITO-PEDOT:PSS device. Based on the knowledge of the device physics we obtained above, the geometry of G_M has been employed for large devices. Also, we note in principle that plastic-aluminium would be a perfectly suitable base substrate and that solution processing of MoOx and Ag have been demonstrated.[14-17] It should also be emphasized that fabricating the 25.0 cm^2 sub-modules presented significant challenges, in particular electrode and contact geometry and achieving uniform spun cast films over such a large area.

Table 1 Performance data, including averages, standard deviations plus the 'hero' MAMS devices of different active areas comprised of P3HT:$PC_{60}BM$ or PCDTBT:$PC_{70}BM$. The results for ITO-PEDOT control devices with the structure ITO/PEDOT:PSS/Photoactive layer/Samarium (Sm)/Al (0.2 cm^2 and 25.0 cm^2) are also listed for comparison.

Cell type	Cell area [cm^2]	V_{OC} [V]	J_{SC} [mA cm^{-2}]	*FF* [%]	R_S [Ω cm^2]	η [%]	
	P3HT:$PC_{60}BM$						Best
MAMS	0.2	0.565±0.012	5.22±0.18	58.7±2.1	26.1±3.1	1.73±0.10	1.84
	2.9	0.567±0.006	4.89±0.27	58.7±2.2	27.0±2.7	1.67±0.10	1.81
	25.0	0.584±0.008	4.56±0.23	50.4±1.5	44.7±4.0	1.35±0.07	1.43
ITO	0.2	0.612±0.004	7.68±0.13	67.7±1.1	12.8±1.2	3.18±0.09	3.31
	25.0	0.545±0.041	5.35±0.19	28.6±0.6	73.3±2.3	0.85±0.03	0.89
	PCDTBT:$PC_{70}BM$						
MAMS	0.2	0.898±0.007	8.54±0.39	54.2±1.5	23.8±2.3	4.16±0.23	4.47
	2.9	0.890±0.023	7.54±0.19	54.1±2.6	27.0±3.7	3.67±0.19	3.90
	25.0	0.900±0.017	7.36±0.24	46.5±2.8	45.4±4.1	3.08±0.19	3.17
ITO	0.2	0.872±0.008	11.12±0.15	56.5±1.1	17.0±0.9	5.48±0.17	5.67
	25.0	0.753±0.031	8.01±0.33	29.0±0.3	71.3±6.3	1.75±0.06	1.80

Figures 8a and 8b show representative *J-V* characteristics of optimised MAMS inverted illumination devices (0.2 cm^2, 2.9 cm^2, 25.0 cm^2) for both photoactive layer acceptor:donor combinations. Also shown are representative control devices with the structure ITO/PEDOT:PSS/Photoactive layer/Samarium (Sm)/Al (0.2 cm^2 and 25.0 cm^2). For 0.2 cm^2 devices we have found that with this architecture conversion efficiencies in excess of 6% with the PCDTBT:$PC_{70}BM$ blend can be generated.[18] Table 1 details the average and highest performance device characteristics (short circuit current density: J_{SC}; open circuit voltage: V_{OC}; Fill Factor: *FF*; and AM1.5 conversion efficiency: η). Also shown are the R_S extracted from the *J-V* slope at open circuit. We can make the following observations from this data: i) in the smallest devices where the anode sheet resistance does not have a major impact, the ITO-PEDOT control cells outperform the MAMS on all key parameters. The device R_Ss are dominated by the extraction dynamics, interface quality and carrier mobility in the active layer. Furthermore, the slightly reduced optical transmittance of the MAMS relative to ITO-PEDOT decreases the current generated. That said, the MAMS PCDTBT:$PC_{70}BM$ cells in particular show very respectable performance; ii) the 2.9 cm^2 MAMS cells display slightly increased R_S as the anode sheet resistance begins to play a role, but maintain *FF*s and critically there is only a small loss in current versus the laboratory-scale device and hence minimal reduction in conversion efficiencies; iii) in the 25.0 cm^2 monolithic sub-modules, the real effect of the anode sheet resistance is manifest – the control ITO-PEDOT devices show a dramatic decrease in all performance parameters and the R_S is more than 1.5 times higher than the MAMS. Furthermore, the V_{OC} is maintained in the large MAMS devices, and although the J_{SC} and *FF*s are slightly reduced likely as a result of pinholes from the spun cast polymer film and a poor Al-active layer interface as a result of the inverse fabrication process, the efficiencies remain at

~80% of the 0.2 cm^2 devices independent of the photoactive materials. In contrast the efficiency for the ITO-PEDOT counterparts is only ~30% of the small devices; iv) the MAMS sub-modules on average show efficiencies > 1.5 times the control ITO-PEDOT devices reaching a maximum of 3.17%. We believe this to be not only the highest reported for an organic solar cell of this geometry (a 25 cm^2 monolithic cell) but also the highest reported for any large area ITO and PEDOT:PSS free device.

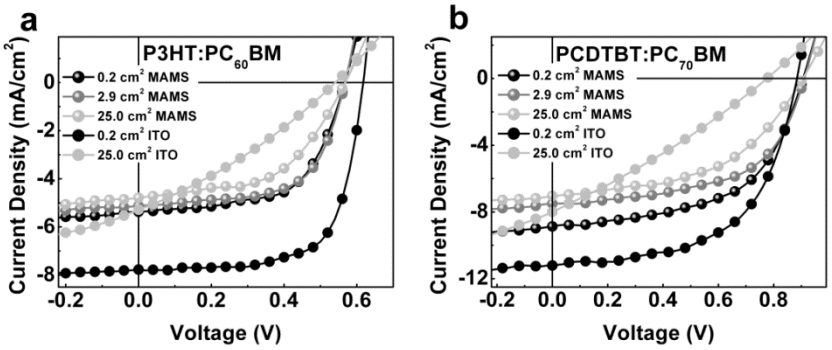

Figure 8 Current density-voltage (*J-V*) characteristics of ITO-PEDOT control cells and MAMS devices fabricated with P3HT:PC_{60}BM (a) and PCDTBT:PC_{70}BM (b) of each active area (0.2 cm^2, 2.9 cm^2, 25.0 cm^2), under AM1.5G illumination from a calibrated solar simulator with irradiation intensity of ~100 mW cm^{-2}.

4. SUMMARY

In summary, three electrode geometries of ITO-based large-area monolithic organic solar cells have been prepared and studied in order to gain insight into series resistance effects – particularly arising from the ITO sheet resistance. The results can be generally applied to other transparent electrodes, and the effect will manifest differentially depending on the scale of sheet resistance. We have shown that the diagonally symmetric G_L design gives the lowest overall performance due to the electric field distribution caused by the electrode geometry. In the diagonal direction for the G_L devices the resistance increases by a factor of two over a 5.6 cm ITO carrier collection path length. The centrally symmetric designs G_M and G_L produced very similar J_{SC} profiles with a higher resistance in the central area leading to lower extracted current. Varying the illumination aperture area revealed the effect of increasing light intensity and also confirmed the manifestations of changes in series resistance from different electrode geometries.

A new transparent, conducting anode with hole-transporting properties suitable for large area organic solar cells has been demonstrated. The anode composed of an optimised MoO_x-Ag-MoO_x stack, showed superior sheet resistance to the current standard ITO-PEDOT:PSS combination (~5 ohm sq^{-1} versus ~15 ohm sq^{-1}) and comparable optical transmittance. The benefit of the MAMS is manifest in large area devices and we have shown in 25.0 cm^2 monolithic sub-cells a maximum power conversion efficiency with and active layer comprised of PCDTBT:PC_{70}BM of 3.2%. Critically, the *FF*s in the large area MAMS devices are maintained relative to the laboratory-scale cells. In contrast the control ITO-PEDOT cells show a dramatic loss in *FF* to < 30%, a factor of 2 lower than the high-efficiency laboratory-scale devices. This is confirmation that at the large scale the power loss in an organic solar cell is derived from the anode whose sheet resistance becomes the only area-scaling parameter. In our case, the efficiency loss depends on the maximum distance the photogenerated current has to flow, that is, 5.0 cm. To our knowledge, a *FF* > 30% in a 25.0 cm^2 organic solar cell has not previously been reported.[19] Furthermore, we have also clearly shown that it is possible to construct high efficiency, high *FF* devices with strip widths > 1.5 cm. This opens new opportunities to create modules and sub-modules with high geometric *FF*s and more efficient use of substrate area. Finally, our MAMS in combination with the proposed inverted illumination geometry presents a viable option for the replacement of the troublesome ITO-PEDOT: PSS duo. The convenience of being able to deposit all layers on a metalized plastic substrate plus the potential to solution deposit the photoactive layer and HTL-anode could dramatically simplify the manufacturing process and drive down \$$watt^{-1}$ production costs of organic solar cells.

5. EXPERIMENTAL SECTION

Materials. PCDTBT (molecular weight, Mn = 65.7 KDa and Mw = 470 KDa) was synthesized and purified in-house following the Suzuki cross-coupling protocols previously described[S1]. P3HT was purchased from Merck while $PC_{60}BM$ and $PC_{70}BM$ were purchased from Nano-C, and MoOx was purchased from Sigma-Aldrich (purity = 99.99%). All commercial products were used as received.

Solutions. For preparing the P3HT:$PC_{60}BM$ devices the solutions of P3HT (32 mg mL-1) and $PC_{60}BM$ (32 mg mL-1) were prepared separately and the equal volumes of the solutions were mixed. For the PCDTBT:$PC_{70}BM$ devices separate solutions of PCDTBT (14 mg mL-1) and $PC_{70}BM$ (56 mg mL-1) were prepared and again equal volumes of the two solutions were mixed before processing. The solvent used in all cases was dichlorobenzene (DCB).

Device Fabrication. The large-area devices for investigating device physics were fabricated on poly(2,3-dihydrothieno-1,4-dioxin)-poly(styrenesulfonate) (PEDOT:PSS) coated 6 cm × 6 cm ITO substrates with a final structure of ITO/PEDOT:PSS/poly(3-n-hexylthiophene) (P3HT):[6,6]-phenyl C61-butyric acid methyl ester ($PC_{60}BM$)/Al. ITO substrates were patterned by photolithography for the three electrode geometries. The PEDOT:PSS (CLEVIOS™ P VP Al 4083) layer of 35-40 nm was spin-coated onto the patterned ITO substrate followed by spin-coating a 1:1 by weight mixture of P3HT and $PC_{60}BM$ in 1,2-dichlorobenzene to give an active layer thickness of 110 nm. Finally, Al was thermally evaporated through a shadow mask to complete the devices and at the same time Al stripes were formed on top of the ITO film free from photoactive layer to reduce the external contact resistance and to connect to the probes. All devices irrespective of the electrode geometry had the same active device area which was defined by the overlap of the ITO electrode, photoactive layer and Al electrode as 5 cm × 5 cm.

ITO & PEDOT-free MAMS organic solar cells were fabricated on bare soda glass substrates (2.5 cm × 2.5 cm and 6.0 cm × 6.0 cm). The cells with active areas of 0.2 and 2.9 cm^2 were fabricated on the smaller substrates and the 25.0 cm^2 cells were fabricated on the larger substrates. The bare glass substrates were first cleaned with detergent, then ultrasonicated in de-ionised water, and subsequently rinsed with acetone and 2-proponal, followed by drying on a hot plate at a temperature of 200 °C for 10 min. The bottom 100 nm Al cathode was deposited by thermal evaporation in a vacuum of ~ 1×10-6 mbar. The P3HT:$PC_{60}BM$ DCB solution was then spun-cast at 1200 rpm to achieve thicknesses of ~110 nm on top of the Al layer. The PCDTBT:$PC_{70}BM$ DCB solution was spun-cast at 1000 rpm to achieve thicknesses of ~110 nm on top of the Al layer. The P3HT:$PC_{60}BM$ films were subsequently heated at 60 °C for 20 min, while the PCDTBT:$PC_{70}BM$ films were heated at 70 °C for 10 min. Finally, 5 nm MoOx, 13 nm Ag and 40 nm MoOx in sequence were subsequently deposited on top of the photoactive layers by thermal deposition in a vacuum of ~ 1×10^{-6} mbar. The active area of 0.2 cm^2 was defined with a shadow mask, while the active areas of 2.9 and 25.0 cm^2 were determined by the overlap of the Al layer and the MAMS. Shadow effects caused by evaporating successive layers of MAMS caused an area error of ~4%, which was taken into account in the measurements of the actual area. After fabrication, conductive Ag paint was applied to the section of the MAMS not overlapped with Al for better circuit contact, followed by annealing at 150°C for 2 minutes.

Thin Film Characterization: All film thicknesses were determined by spectroscopic ellipsometry (J. A. Woollam Co., Inc.) and independently measured with a Veeco Dektak 150 surface profilometer. The absorption and transmission spectra were recorded by using a UV-Vis-NIR spectrophotometer (Cary 5000). The sheet resistance was determined by micro-controlled four-probe meter from Sevenstar.

Calibration and Device Measurements: The solar simulator (Abet Triple-A from Abet Technologies) was calibrated by carefully minimizing the solar mismatch of the Xenon lamp (550 W Oriel) spectrum using an AM1.5G filter. The light intensity at ~100 mW cm^{-2} AM1.5G was also calibrated by using a National Renewable Energy Laboratory (NREL)-certified standard 2 cm × 2 cm silicon photodiode with a KG5 filter. Within the illumination area of 5 cm × 5 cm, the variation of the light intensity was below 3% as measured by mapping with a calibrated photodiode. All measurements were made in an MBraun nitrogen glove box (O_2 < 0.1 ppm; H_2O < 0.1 ppm). Current density-voltage curves were measured with a Keithley 2400 source measurement unit. Incident Photon Conversion Efficiency (IPCE) spectra were recorded with a PV Measurement QEX7 setup, which was calibrated by an NREL certified photodiode and operated without white light bias and chopped and locked in the small perturbation limit.

Computational Modeling: Modeling of the current density in the ITO electrode was performed using COMSOL (AC/DC module). A two dimensional model of the electrode was created consisting of ~4000 elements with a uniform electrical conductivity of 1×10^6 S m-1, which is typical for sputtered ITO thin films.[20] The test voltage was applied to the edges

of the electrode, adjacent to the probe head, by selecting the 'electric potential' boundary condition. For the other edges the 'distributed resistance' boundary condition was used to simulate the interface between the electrode and the active layer above.

REFERENCES

[1] Green, M. A., Emery, K., Hishikawa, Y., Warta, W., and Dunlop, E. D., "Solar cell efficiency tables (version 39)," Prog. Photovolt: Res. Appl. Papers 20, 12 (2012).

[2] Muhsin, B., Renz, J., Drüe, K.-H., Gobsch, G., and Hoppe, H., "Influence of polymer solar cell geometry on series resistance and device efficiency," Phys. Status Solidi A 206, 2771 (2009).

[3] Gupta, D., Bag, M., and Narayan, K. S., "Area dependent efficiency of organic solar cells," Appl. Phys. Lett. 93, 163301 (2008).

[4] Brewer, S. H., and Franzen, S. "Optical properties of indium tin oxide and fluorine-doped tin oxide surfaces: correlation of reflectivity, skin depth, and plasmon frequency with conductivity," J. Alloys Compd. 338, 73 (2002).

[5] Balestrieri, M., Pysch, D., Becker, J.-P., Hermle, M., Warta, W., and Glunz, S. W. "Characterization and optimization of indium tin oxide films for heterojunction solar cells," Sol. Energy Mater. Sol. Cells 95, 2390 (2011).

[6] Jin, H., Pivrikas, A., Lee, K. H., Aljada, M., Hambsch, M., Burn, Paul L., and Meredith, P. "Factors influencing the efficiency of current collection in large area, monolithic organic solar cells," Adv. Energy Mater. DOI: 10.1002/aenm.201200254 (2012).

[7] Choi, S., Potscavage, W. J., and Kippelen, Jr., B. "Area-scaling of organic solar cells," J. Appl. Phys. 106, 054507 (2009).

[8] Jin, H., Tao, C., Velusamy, M., Aljada, M., Zhang, Y., Hambsch, M., Burn, P. L. and Meredith, P. "Efficient, large area ITO-and-PEDOT-free organic solar cell sub-modules," Adv. Mater. 24, 2572 (2012).

[9] Sun, Y., Takacs, C. J., Cowan, S. R., Seo, J. H., Gong, X., Roy, A. and Heeger, A. J. "Efficient, air-stable bulk heterojunction polymer solar cells using MoOx as the anode interfacial layer," Adv. Mater. 23, 2226 (2011).

[10] Persson, N.-K., Arwin, H., Inganäs, O. "Optical optimization of polyfluorene-fullerene blend photodiodes," J. Appl. Phys. 97, 034503 (2005).

[11] Pettersson, L. A. A., Roman, L. S., and Inganäs, O. "Modeling photocurrent action spectra of photovoltaic devices based on organic thin films," J. Appl. Phys. 86, 487 (1999).

[12] Tao, C., Xie, G., Meng, F., Ruan, S., and Chen, W. "Tailoring spatial distribution of the optical field intensity in semitransparent inverted organic solar cells," J. Phys. Chem. C 115, 12611 (2011).

[13] Moulé, A. J., and Meerholz, K. "Intensity-dependent photocurrent generation at the anode in bulk-heterojunction solar cells," Appl. Phys. B 92, 209 (2008).

[14] Manceau, M., Angmo, D., Jørgensen, M., and Krebs, F. C. "ITO-free flexible polymer solar cells: From small model devices to roll-to-roll processed large modules," Org. Electron. 12, 566 (2011).

[15] Hu, L., Kim, H. S., Lee, J. Y., Peumans, P., and Cui, Y. "Scalable coating and properties of transparent, flexible, silver nanowire electrodes," ACS Nano 4, 2995 (2010).

[16] Stubhan, T., Ameri, T., Salinas, M., Krantz, J., Machui, F., Halik, M., and Brabec, C. J. "High shunt resistance in polymer solar cells comprising a MoO_3 hole extraction layer processed from nanoparticle suspension," Appl. Phys. Lett. 98, 253308 (2011).

[17] Meyer, J., Khalandovsky, R., Görrn, P., and Kahn, A. "MoO_3 films spin-coated from a nanoparticle suspension for efficient hole-injection in organic electronics," Adv. Mater. 23, 70 (2011).

[18] Pandey, A. K., Aljada, M., Velusamy, M., Burn, P. L., and Meredith, P. "Nanostructured, active organic–metal junctions for highly efficient charge generation and extraction in polymer-fullerene solar cells," Adv. Mater. 24, 1055 (2012).

[19] Jeong, W.-I., Lee, J., Park, S.-Y., Kang, J.-W., and Kim, J.-J. "Reduction of collection effi ciency of charge carriers with increasing cell size in polymer bulk heterojunction solar cells," Adv. Funct. Mater. 21, 343 (2011).

[20] Granqvist, C. G., and Hultåker, A. "Transparent and conducting ITO films: new developments and applications," Thin Solid Films 411, 1 (2002).